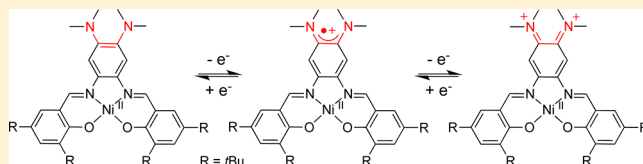


Reversible Double Oxidation and Protonation of the Non-Innocent Bridge in a Nickel(II) Salophen Complex

David de Bellefeuille,[†] Mohammad S. Askari,[†] Benedikt Lassalle-Kaiser,[‡] Yves Journaux,^{‡,§} Ally Aukauloo,[‡] Maylis Orio,[⊥] Fabrice Thomas,^{*,||} and Xavier Ottenwaelder^{*,†}[†]Department of Chemistry and Biochemistry, Concordia University, Montreal, Quebec H4B 1R6, Canada[‡]Institut de Chimie Moléculaire et des Matériaux d'Orsay, UMR CNRS 8182, Université Paris-Sud, 91405 Orsay, France[§]Institut Parisien de Chimie Moléculaire, UMR CNRS 7201, Université Pierre et Marie Curie-Paris 6, 75252 Paris Cedex 05, France[⊥]Laboratoire de Spectrochimie Infrarouge et Raman, UMR CNRS 8516, Université des Sciences et Technologies de Lille, 59655 Villeneuve d'Ascq Cedex, France^{||}Département de Chimie Moléculaire, UMR CNRS 5250, Université Joseph Fourier, 38041 Grenoble Cedex 9, France

S Supporting Information

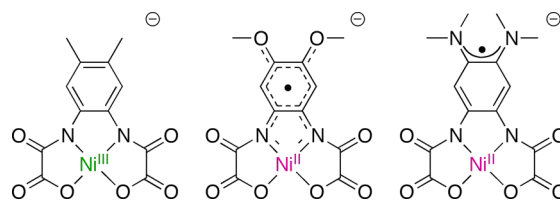
ABSTRACT: Substitution on the aromatic bridge of a nickel(II) salophen complex with electron-donating dimethylamino substituents creates a ligand with three stable, easily and reversibly accessible oxidation states. The one-electron-oxidized product is characterized as a nickel(II) radical complex with the radical bore by the central substituted aromatic ring, in contrast to other nickel(II) salen or salophen complexes that oxidize on the phenolate moieties. The doubly oxidized product, a singlet species, is best described as having an iminobenzoquinone bridge with a vinylogous distribution of bond lengths between the dimethylamino substituents. Protonation of the dimethylamino substituents inhibits these redox processes on the time scale of cyclovoltammetry, but electrolysis and chemical oxidation are consistent with deprotonation occurring concomitantly with electron transfer to yield the mono- and dioxidized species described above.



■ INTRODUCTION

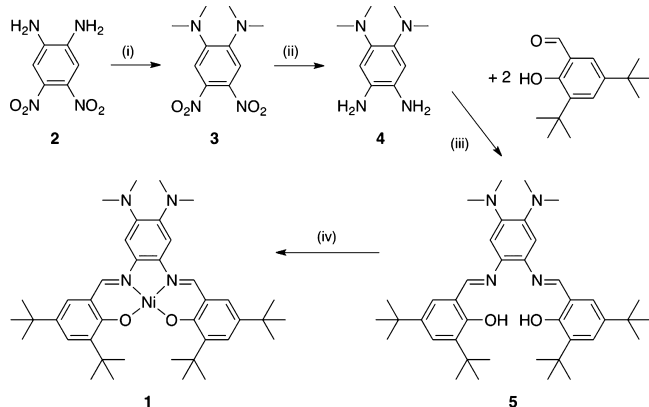
Combining the redox properties of a metal ion and an organic moiety constitutes an elegant methodology to access high formal oxidation states when the metal ion alone is insufficient to undergo all catalytic redox steps.^{1,2} In metalloenzymes, organic cofactors such as the porphyrin of hemic systems³ and tyrosine residues⁴ can thus be transiently oxidized to radicals and promote efficient catalytic turnover. In chemical modeling, a number of ligand types are redox-active (non-innocent) when engaged within a complex,^{4,5} e.g., porphyrins,⁶ phenolates,^{7,8} catecholates,⁹ aminophenolates,¹⁰ phenylenediamines,¹¹ benzene-*N*-amidates,^{12–15} and diimines.¹⁶ In complexes with a non-innocent ligand, the locus of oxidation (or reduction) is dictated by the respective symmetry and energy of the frontier orbitals of the metal ion and those of the organic framework.¹¹ Thus, the oxidation site in a complex can be shifted from the metal to the ligand by tuning the electronics of the ligand. Our group previously investigated the oxidative chemistry of nickel(II) phenylenediaminebis(oxamato) complexes (Scheme 1), where the aromatic ligand harbors substituents of various electron-donating properties. The strongly electron-donating dimethylamino (NMe₂) substituents direct the oxidation site toward the aromatic part of the ligand, whereas a metal-centered oxidation process is observed for the parent, unsubstituted complex.¹⁴ From a fundamental point of view, identifying new types of metalloradical complexes will comple-

Scheme 1. Tuning the Redox Properties of an Aromatic Ligand by Appropriate Substitution, from a Nickel(III) Complex to a Delocalized Nickel(II) Radical Species to a Pure Radical Species¹⁴



ment our knowledge of these intriguing species. In the present paper, we investigate the oxidative chemistry of the nickel(II) complex **1** of the novel salophen ligand 4,5-bis-(dimethylamino)benzene-1,2-bis(3,5-di-*tert*-butylsalicylimine) (**5**), which incorporates a (NMe₂)₂-substituted aromatic bridge. We show that **1** undergoes two ligand-based, low-potential, reversible oxidations to yield a phenylenediamine radical, **1**^{•+}, and an α -diiminoquinone species, **1**²⁺, both being stable for hours (Scheme 2).

Received: July 31, 2012

Scheme 2. Synthetic Route toward **1**^a

^a(i) $(\text{CH}_2\text{O})_m$, NaBH_3CN , AcOH , 89%; (ii) H_2 , Pd/C , MeOH , quantitative; (iii) HC(OMe)_3 , MeOH , 67%; (iv) Ni(OAc)_2 , $\text{CH}_2\text{Cl}_2/\text{MeOH}$, 96%.

RESULTS AND DISCUSSION

Synthesis and Structures of the Ligand and Neutral Nickel(II) Complex. The synthesis of **5** is based on 4,5-diamino-1,2-dinitrobenzene (**2**),¹⁷ a versatile precursor for tetraminobenzene rings that are differently substituted at the 1,2 versus the 4,5 positions (Scheme 1).^{14,18,19} Metalation of **5** with nickel(II) acetate affords **1**, a diamagnetic complex, as evidenced by sharp NMR signals both in CDCl_3 and in dimethyl sulfoxide ($\text{DMSO}-d_6$). The aromatic protons H3 and H6 of **1** are more shielded (7.02 ppm) than those in the MeO-substituted (7.1 ppm)²⁰ or Me-substituted (7.44 ppm)²¹ nickel(II) salophen complexes, indicating that the central ring is electron-rich owing to the NMe_2 substituents. The crystal structure of **1** reveals the expected square-planar coordination environment that is typical of nickel(II) in a salophen cavity (Figure 1 and Table 1).^{20–22} A small puckering is induced by

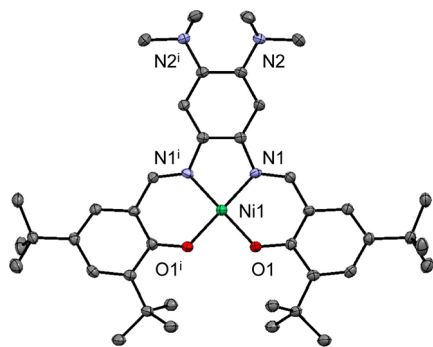


Figure 1. ORTEP representation at 50% ellipsoid probability of **1** (i: x , y , 0.5 – z). Hydrogen atoms were omitted for clarity. Selected bond lengths: Ni1–N1 , 1.8504(17) Å; Ni1–O1 , 1.8475(14) Å.

steric contact between the 6-*tert*-butyl substituents, as evidenced by a ca. 13° angle between the average planes defined by the central ring and each phenolate and a ca. 29° angle between the average phenolate planes. Because of steric contact between the methyl groups of distinct NMe_2 substituents, the angle between the NMe_2 groups and the mean benzene plane is 55° in this solid-state structure, denoting limited resonance.

Electrochemistry. The electrochemical behavior of the ligand and complexes has been studied in CH_2Cl_2 (+0.1 M

Table 1. Crystallographic Data for **1** and $[\text{1H}](\text{SbF}_6)$

	1	$[\text{1H}](\text{SbF}_6)$
CCDC number	893505	893506
empirical formula	$\text{C}_{40}\text{H}_{36}\text{N}_4\text{NiO}_2$	$\text{C}_{40}\text{H}_{37}\text{F}_6\text{N}_4\text{NiO}_2\text{Sb}$
fw	683.60	920.36
temperature (K)	110(2)	110(2)
wavelength (Å)	1.54178	1.54178
cryst syst	monoclinic	monoclinic
space group	$C2/c$	$P2_1/c$
a (Å)	23.9521(7)	15.5147(3)
b (Å)	15.1711(4)	9.0739(2)
c (Å)	10.3912(3)	32.0739(6)
α (deg)	90	90
β (deg)	101.883(2)	111.3800(10)
γ (deg)	90	90
volume (Å ³)	3695.03(18)	4204.59(15)
Z	4	4
density (calcd)	1.229	1.454
abs coeff	1.049	6.201
$F(000)$	1472	1896
cryst size (mm ³)	$0.03 \times 0.05 \times 0.56$	$0.04 \times 0.07 \times 0.42$
index ranges	$h = -28 \rightarrow +28, k = -18 \rightarrow +17, l = -12 \rightarrow +12$	$h = -18 \rightarrow +18, k = -10 \rightarrow +10, l = -38 \rightarrow +38$
reflns collected	16344	56704
independent reflns	3334	7678
param	221	506
GOF	1.048	1.094
final R indices [$I > 2\sigma(I)$]	$R1 = 4.14\%$, $wR2 = 9.76\%$	$R1 = 3.826\%$, $wR2 = 9.30\%$
R indices (all data)	$R1 = 6.82\%$, $wR2 = 11.11\%$	$R1 = 4.68\%$, $wR2 = 9.70\%$
largest diff peak and hole (e/Å ³)	0.535 and -0.457	1.072 and -1.058

$n\text{Bu}_4\text{NClO}_4$ as the supporting electrolyte) by cyclic voltammetry, differential pulse voltammetry, and rotating-disk electrode (RDE) voltammetry. All potentials are referenced versus the Fc^+/Fc couple.

The cyclovoltammogram (CV) of the free ligand **5** in CH_2Cl_2 displays two oxidation waves at $E_{1/2}^1 = 0.07$ V ($\Delta E_p = 0.06$ V) and $E_{1/2}^2 = 0.25$ V ($\Delta E_p = 0.06$ V), each corresponding to a one-electron process (Figure S1 in the Supporting Information, SI). The first redox transfer is reversible, showing that the stability of the cation is noteworthy. In contrast, the low I_p^a/I_p^c value for the second wave indicates that the dication is rather unstable, at least on the time scale of the experiment. Both oxidations of **5** occur at much lower potentials than those for the phenoxyl/phenol couples in the parent salophen ligand (unsubstituted at the central ring, 0.74 V) and related salen ligands involving di-*tert*-butylphenol moieties (0.65–0.80 V).²³ $E_{1/2}^1$ and $E_{1/2}^2$ values for **5** are, however, within the range of those measured for the oxidation of a series of $(\text{NMe}_2)_2$ -substituted aromatic derivatives. For example, oxidation of 1,4,5,8-tetrakis(dimethylamino)naphthalene occurs at $E_{1/2}^1 = -0.01$ and $E_{1/2}^2 = 0.07$ V, oxidation of 2,3,6,7-tetrakis(dimethylamino)naphthalene occurs at $E_{1/2}^1 = 0.08$ and $E_{1/2}^2 = 0.16$ V,^{24,25} and N,N,N',N' -tetramethyl-*p*-phenylenediamine exhibits oxidation potentials of -0.21 and 0.38 V, the first one yielding the famous Würster's Blue salt.²⁶ The electron transfers observed for **5** are thus ascribed to sequential oxidations on the central tetraminobenzene ring into a radical cation and then a closed-shell α -diiminoquinone dication.

The CV of the nickel(II) complex **1** in CH_2Cl_2 (Figures 2 and S2 and S3 in the SI) displays three quasi-reversible one-

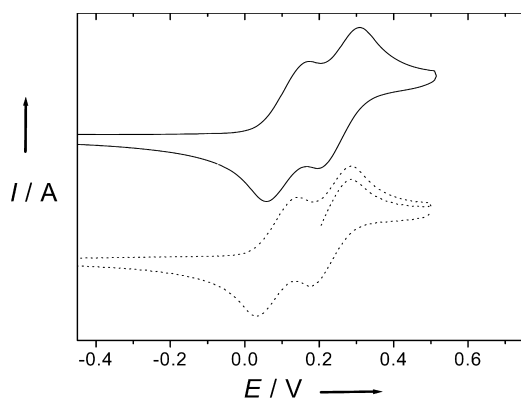


Figure 2. CV traces of 1 mM CH_2Cl_2 solutions (+0.1 M $n\text{Bu}_4\text{NClO}_4$) of **1** (—) and electrogenerated 1^+ (···) at a carbon working electrode. Potentials are relative to the Fc^+/Fc redox couple. Scan rate = 0.1 V/s. $T = 298 \text{ K}$.

electron oxidation waves at $E_{1/2}^1 = 0.12$ (peak-to-peak separation $\Delta E_p = E_p^{a1} - E_p^{c1} = 0.11 \text{ V}$), $E_{1/2}^2 = 0.24 \text{ V}$ ($\Delta E_p = 0.11 \text{ V}$), and $E_{1/2}^3 = 0.97 \text{ V}$ ($\Delta E_p = 0.12 \text{ V}$). Typically, symmetrical nickel(II) salen complexes with two di-*tert*-butylphenolate moieties exhibit two quasi-reversible one-electron oxidation waves above 0.4 V, which correspond to the successive oxidations of the phenolate moieties into phenoxyl radicals.^{20–22,27–31} The low values of $E_{1/2}^1$ and $E_{1/2}^2$ of **1** advocate for a different assignment, e.g., successive oxidations of the tetraaminobenzene central ring. This hypothesis is further supported by the close similarity between the oxidation potentials of **1** and the free ligand **5**. The third redox wave of **1** is likely centered on the phenolate moieties, but it has not been further investigated because of the low stability of the trication 1^{3+} .

For spectroscopic characterization, oxidized species 1^+ and 1^{2+} were prepared either by bulk electrolysis at a fixed potential of 0.20 or 0.42 V, respectively, or by chemical oxidation using 1 equiv of acetylferrocenium ($E^\circ = 0.27 \text{ V}$) or 2 equiv of 1,1'-diacetylferrocenium ($E^\circ = 0.49 \text{ V}$) in CH_2Cl_2 , respectively.³² Given the proximity of the first two oxidation processes of **1**, 1^+ disproportionates to **1** and 1^{2+} with an equilibrium constant of ca. 1.0×10^{-3} . A solution sample of 1^+ would thus contain $\sim 3\%$ of each **1** and 1^{2+} . This phenomenon was taken into account during analysis of the spectroscopic data. Both preparation methods gave similar results, but the oxidized species were more stable timewise under the chemical oxidation conditions. For example, a solution of dication 1^{2+} , obtained via chemical oxidation, was left standing for 4 h under an inert atmosphere. Further reduction of this solution with ferrocene and analysis of the products after chromatography indicated $>95\%$ recovery of **1**, thus evidencing a noticeable stability of the dication.

Electron Paramagnetic Resonance (EPR) Spectroscopy. The 25 K EPR spectrum of 1^+ in CH_2Cl_2 consists of an isotropic ($S = 1/2$) radical signal centered at $g_{\text{iso}} = 2.004$ (Figure S4 in the SI). This suggests a lack of metal character in the singly occupied molecular orbital (SOMO) of 1^+ and argues against a nickel(II) phenoxyl radical formulation because such species are known to have higher g_{iso} values (typically 2.03 for salen precursors involving 2,4-di-*tert*-butylphenolate moieties).^{20–22,27–31} More information about the oxidation site in

1^+ is provided by its isotropic EPR spectrum in CH_2Cl_2 at 293 K (Figure 3). Under these conditions, the $S = 1/2$ signal is still

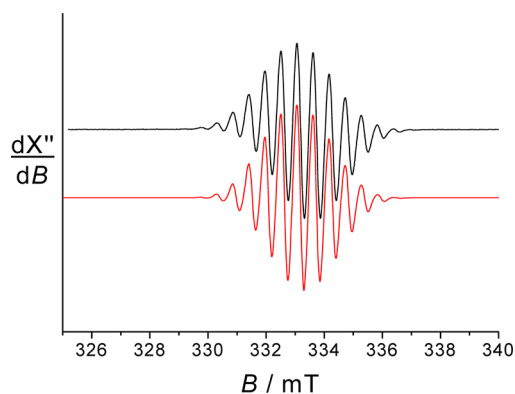
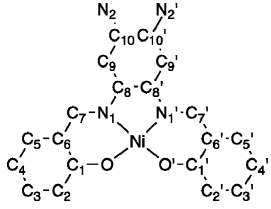


Figure 3. X-band EPR spectrum of the electrochemically generated 1^+ in CH_2Cl_2 . Black lines: experimental spectrum. Red lines: simulation using the parameters given in the text. $T = 293 \text{ K}$. Microwave power = 4 mW. Microwave frequency = 9.33 GHz. Modulation amplitude = 0.05 mT. Modulation frequency = 100 kHz.

observed at $g_{\text{iso}} = 2.004$, but a hyperfine splitting due to the interaction of the electron spin with hydrogen and nitrogen nuclei could be evidenced. From simulation of the spectrum, the following isotropic hyperfine coupling (HFC) constants were obtained: 13.7 MHz for six equivalent ^1H nuclei, 17.7 MHz for six equivalent ^1H nuclei, and 14.4 MHz for two equivalent ^{14}N nuclei. The high HFC values to nitrogen atoms rule out phenoxyl character for the radical species. Instead, the HFC pattern indicates that the radical is delocalized over the two NMe_2 substituents without significant contribution of either iminic nitrogen atoms or the nickel center.^{26,33} We calculated the EPR parameters by density functional theory (DFT) methods with the ORCA program package (see below for more computational details). The calculated HFC constants are $A_{6\text{H}} = 13.7 \text{ MHz}$, $A_{6\text{H}} = 16.7 \text{ MHz}$, and $A_{2\text{N}} = 12.9 \text{ MHz}$, with a highly isotropic g matrix ($g_1 = 2.0018$, $g_2 = 2.0047$, and $g_3 = 2.0065$; $g_{\text{iso}} \sim 2.004$). The very good agreement between experimental and theoretical EPR data confirms the assignment of 1^+ as a π -radical localized on the central bis(dimethylamino)-benzene ring.³⁴

The dication 1^{2+} is EPR-silent in CH_2Cl_2 at both 20 and 100 K, consistent with a diamagnetic character of the doubly oxidized ligand (see below).

DFT Calculations. DFT calculations were undertaken at the B3LYP level of theory with the ORCA package in order to gain insight into the geometric and electronic structures of the oxidized species. The structures of the oxidized species 1^+ and 1^{2+} and protonated radical 1H^{2+} , as well as the initial complexes **1** and 1H^+ for comparison, were investigated by geometry optimization. Except for the putative radical species 1H^{2+} (chemically irrelevant; see below for protonation studies), the optimized structures were found to be symmetrical. A reasonable agreement was found between the calculated and experimental bond lengths for complexes **1** (Table 2 and Figure S9 in the SI) and 1H^+ (Table S1 and Figure S11 in the SI). In the case of 1^{2+} , the electronic description is complicated by the need to consider two spin states, singlet and triplet, hereafter denoted as $^11^{2+}$ and $^31^{2+}$, respectively (Figure S10 in the SI). We calculated the energy gap between the optimized singlet and triplet forms and found that the singlet was stabilized by

Table 2. Selected Experimental and Calculated Bond Lengths (Å) for **1**, **1⁺**, and **1²⁺**


bond	nature				
	closed shell		radical	singlet closed shell	triplet open shell
	1 (exptl)	1 (calcd)	1⁺ (calcd)	1²⁺ (calcd)	3¹1²⁺ (calcd)
Ni–O	1.848	1.883	1.881	1.890	1.869
Ni–N1	1.850	1.885	1.884	1.895	1.875
C1–O1	1.310	1.299	1.291	1.280	1.287
C1–C2	1.438	1.444	1.446	1.448	1.449
C2–C3	1.379	1.382	1.378	1.373	1.378
C3–C4	1.412	1.418	1.425	1.435	1.421
C4–C5	1.369	1.371	1.366	1.360	1.380
C5–C6	1.419	1.420	1.426	1.432	1.407
C1–C6	1.419	1.430	1.440	1.457	1.444
C6–C7	1.420	1.417	1.403	1.386	1.412
C7–N1	1.310	1.305	1.317	1.364	1.309
N1–C8	1.419	1.414	1.395	1.364	1.407
C8–C9	1.394	1.398	1.383	1.379	1.377
C9–C10	1.387	1.395	1.407	1.411	1.413
C10–C10'	1.428	1.440	1.462	1.500	1.460
C8–C8'	1.382	1.393	1.427	1.472	1.420
C10–N2	1.420	1.408	1.365	1.325	1.358

13.0 kJ/mol (including solvation terms). Therefore, the singlet is likely the ground spin state of **1²⁺**.

Metrical analysis of the calculated **1** and **1⁺** structures supports the locus of oxidation being on the central ring (Table 2 and Figure S9 in the SI). Examination of the C–C and C–O bond lengths within the phenolic rings of **1** and **1⁺** reveals that no significant change occurs upon oxidation, with the bond lengths being similar within ± 0.01 Å and the N–Ni and O–Ni bond lengths not varying by more than 0.002 Å. The C–C and C–O bond lengths in the phenolic rings of **1⁺** are all in the range expected for bis(phenolate) character. In contrast, clear metrical changes are observed within the bis(dimethylamino)-benzene fragment on going from **1** to **1⁺** (Table 2). The shortening of the C10–N2 and C8–C9 bonds, concomitant with the lengthening of C10–C10' and C8–C8', highlights a quinoidal distribution of bond lengths within the tetramino-benzene ring in **1⁺**.³⁵ This is strong evidence that oxidation of **1** occurs on the bridge, affording a phenylene π radical **1⁺**.

Interestingly, the magnitude of the C10–N2 shortening (0.043 Å) is much larger than that for the C8–N1 bonds (0.019 Å), suggesting that the radical character in **1⁺** resides on the 4,5-diaminobenzene fragment rather than the 1,2,4,5-tetramino-benzene fragment.

The energetically favored singlet spin state of **1²⁺**, **1¹1²⁺**, displays phenolic C–C and C–O bond lengths that are very close to those calculated for **1** and **1⁺** and thus has bis(phenolate) character (Table 2 and Figure S10 in the SI). The bonds in the central ring of **1¹1²⁺** display the same trend that was observed on going from **1** to **1⁺**, i.e., α -diiminoquinone character showing that double oxidation occurs on the electron-rich bridge of **1**. The angles between the NMe₂ substituents and the central ring in both **1⁺** and **1¹1²⁺** are small (18 and 14°, respectively) compared with that in **1** (55°), evidencing a strong participation of the NMe₂ groups in the resonance stabilization of the oxidized species.³⁶

The geometric structure of triplet **1²⁺**, **3¹1²⁺**, is consistent with diradical character (Table 2 and Figure S10 in the SI). A comparison of the metrical parameters of **3¹1²⁺** with those of **1⁺** shows that some bonds within the phenolic rings are altered by oxidation: in particular, C5–C6 is shortened by 0.019 Å, and C4–C5 is lengthened by 0.015 Å. These features are indicative of phenoxyl character for **3¹1²⁺**,³⁵ with the radical being equally shared between the two peripheral rings of the molecule. In agreement with this assumption, a comparison of the bond lengths within the central radical rings of **1⁺** and **3¹1²⁺** does not reveal any significant difference. Therefore, **3¹1²⁺** is better described as a diradical involving both delocalized phenoxyl moieties and a bis(dimethylamino)benzene π -radical unit.

Consistent with the metrical analysis, the calculated SOMO of **1⁺** is essentially located on the bis(dimethylamino)benzene fragment (75%) with a small contribution from the salicylimines (25%; Figure 4a). Not surprisingly, the lowest unoccupied molecular orbital (LUMO) of the singlet dication **1¹1²⁺** corresponds to the SOMO of **1⁺** (Figure 4b; 75% bis(dimethylamino)benzene fragment and 25% salicylimines). The two SOMOs of the triplet diradical **3¹1²⁺** are shown in Figure 4c. One has a main bis(dimethylamino)benzene character (95%), with a small contribution of the salicylimines (5%). The other has a main salicylimine character (85%), with small contributions of the bis(dimethylamino)benzene central ring (5%) and a nickel d_{xz} orbital (10%).

The individual atomic contributions to the spin density confirm the assignments made above (Table 3 and Figure S12 in the SI). In **1⁺**, the spin density is found exclusively on the central ring and the nitrogen atoms of the NMe₂ substituents, with negligible contribution from the phenolate or imine moieties. In the case of **3¹1²⁺**, the spin populations are essentially the same on the central ring and NMe₂ substituents as those in

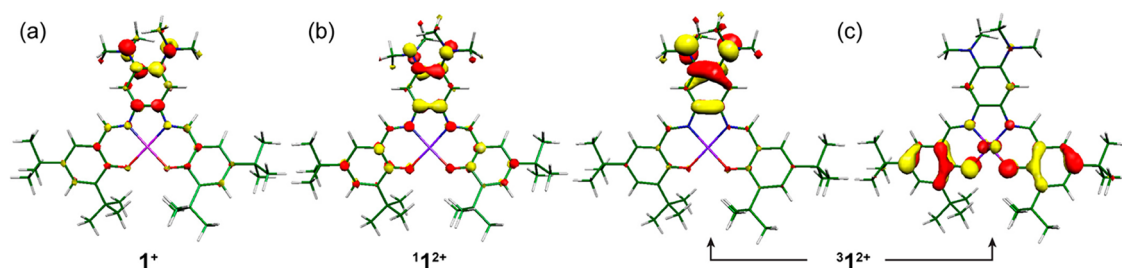
**Figure 4.** Localized MOs: (a) SOMO of **1⁺**; (b) LUMO of singlet **1¹1²⁺**; (c) SOMOs for triplet diradical **3¹1²⁺**. See text for fragment composition.

Table 3. Individual Contributions of the Atoms to the Spin Density in 1^+ and Triplet $^31^{2+}$

atom	1^+	$^31^{2+}$	atom	1^+	$^31^{2+}$
Ni	0	0.10	C5	0	0
O	0	0.15	C6	0.02	0.10
N1	0.02	0	C7	0.02	0
C1	0	0	C8	0.11	0.07
C2	0	0.06	C9	0	0
C3	0	0	C10	0.10	0.09
C4	0	0.13	N2	0.22	0.26

^aSee Table 2 for atom numbering.

1^+ , with the addition of radical character on the phenolic moieties, thereby confirming this species as a multisite diradical.

Electronic Spectra and Time-Dependent DFT (TD-DFT) Calculations. Oxidation of **1** to 1^+ and 1^{2+} leads to drastic changes in the electronic absorption spectra. In contrast to **1**, both orange-brown 1^+ and brown 1^{2+} exhibit intense absorptions in the vis–near-IR (NIR) range (Figure 5 and

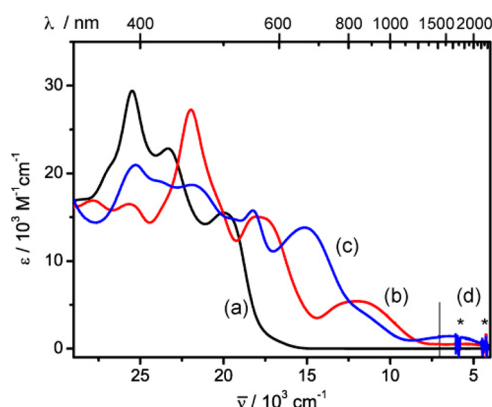


Figure 5. UV–vis–NIR spectra of **1** (a, black), 1^+ (b, red), and 1^{2+} (c, blue) generated by spectroelectrolysis at -30°C (1 mM CH_2Cl_2 and 0.1 M TBAPF₆). (d) Extension of the spectra in the 1400–2800 nm range as per chemical oxidation of **1** with Ac_2Fc^+ in CH_2Cl_2 . The asterisks denote solvent absorptions.

Table 4). The extinction coefficients of these absorptions are reminiscent of charge-transfer (CT) bands. It is worth noting that 1^+ displays no significant absorption at wavenumbers lower than 8000 cm^{-1} (Figure 5b), in sharp contrast with the nickel(II) phenoxyl radical salen complexes, which typically exhibit an intense intervalence charge-transfer (IVCT) band at $4300\text{--}4700\text{ cm}^{-1}$ ($17\text{--}25\text{ mM}^{-1}\text{ cm}^{-1}$).^{28–31} The red shift of the vis–NIR features of 1^{2+} (Figure 5c) compared with 1^+ likely reflects an increase in the ligand oxidation state.

The UV–vis–NIR spectrum of the radical cation 1^+ is well matched by the electronic excitations predicted by TD-DFT calculations (Table 4). In particular, the calculations confirm the absence of an intense IVCT transition in the NIR that would have indicated a mixed-valence phenolate–phenoxyl radical system.^{28–31} The three lowest-energy absorptions are rising from interligand charge-transfer (ILCT) transitions (Figure 6). In the $\beta\text{HOMO} \rightarrow \beta\text{LUMO}$ transition (HOMO = highest occupied molecular orbital) at 11592 cm^{-1} , the donor orbital is a π system mainly located on the phenolate rings, while the acceptor orbital (βLUMO) is principally located on the central bis(dimethylamino)benzene fragment with a small contribution from the phenolate moieties. The next two

Table 4. Electronic Transitions of 1^+ and 1^{2+} (Singlet, $^11^{2+}$; Triplet, $^31^{2+}$)

	experimental	TD-DFT	
	ν, cm^{-1} ($\epsilon, \text{M}^{-1}\text{cm}^{-1}$)	ν, cm^{-1} (f)	assignment ^a
1^+	12000 (5410)	11592 (0.019)	$\beta\text{HOMO} \rightarrow \beta\text{LUMO}$, IL
	18000 (15000)	18112 (0.120)	$\beta\text{HOMO}-1 \rightarrow \beta\text{LUMO}$, IL
	22000 (27300)	24409 (0.307)	$\beta\text{HOMO}-3 \rightarrow \beta\text{LUMO}$, IL
$^11^{2+}$	6250 (1430)	5777 (0.102)	$\beta\text{HOMO} \rightarrow \beta\text{LUMO}$, IL
	12000 (shoulder)	12991 (0.011)	$\beta\text{HOMO}-2 \rightarrow \beta\text{LUMO}$, IL
	15100 (13800)	16674 (0.145)	$\beta\text{HOMO}-3 \rightarrow \beta\text{LUMO}$, IL
	18250 (15750)	18988 (0.171)	$\beta\text{HOMO}-7 \rightarrow \beta\text{LUMO}$, ML
$^31^{2+}$		6920 (0.26)	$\beta\text{HOMO} \rightarrow \beta\text{LUMO}$, IL
		10316 (0.15)	$\beta\text{HOMO}-1 \rightarrow \beta\text{LUMO}$, ML

^aIL = intraligand charge transfer. ML = metal-to-ligand charge transfer.

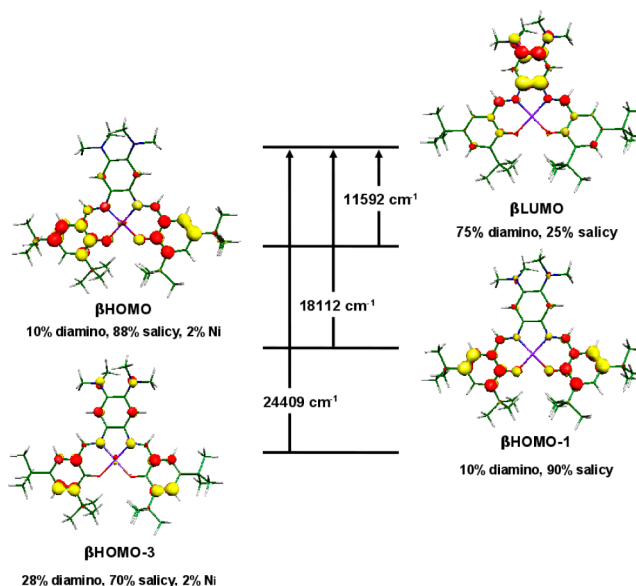


Figure 6. TD-DFT assignment of the main electronic excitations of 1^+ , with fragment population of the relevant MOs. Fragments: Ni = nickel atom; salicy = salicylimine moieties (phenolate rings + imines); diamino = central ring + NMe_2 substituents.

absorptions stem from $\beta\text{HOMO}-1 \rightarrow \beta\text{LUMO}$ and $\beta\text{HOMO}-3 \rightarrow \beta\text{LUMO}$ transitions, respectively. The donor orbitals are again ligand-centered, with $\beta\text{HOMO}-1$ being a π system mainly located on the phenolate rings and $\beta\text{HOMO}-3$ being a π system delocalized over the whole salophen backbone with dominant contributions of the phenolates and central ring.

TD-DFT calculations on 1^{2+} were conducted by considering both the singlet and triplet spin states (Table 4). Only the set of excitations for the singlet species reproduced the experimental bands, thus confirming the singlet nature of 1^{2+} . A detailed analysis of the composition of the molecular orbitals (MOs) involved in the transitions reveals that the absorptions at 6250, 12000, and 15100 cm^{-1} stem from ILCT transitions, while the band at 18250 cm^{-1} corresponds to a metal-to-ligand charge-transfer (MLCT) transition (Figure 7). In particular, the

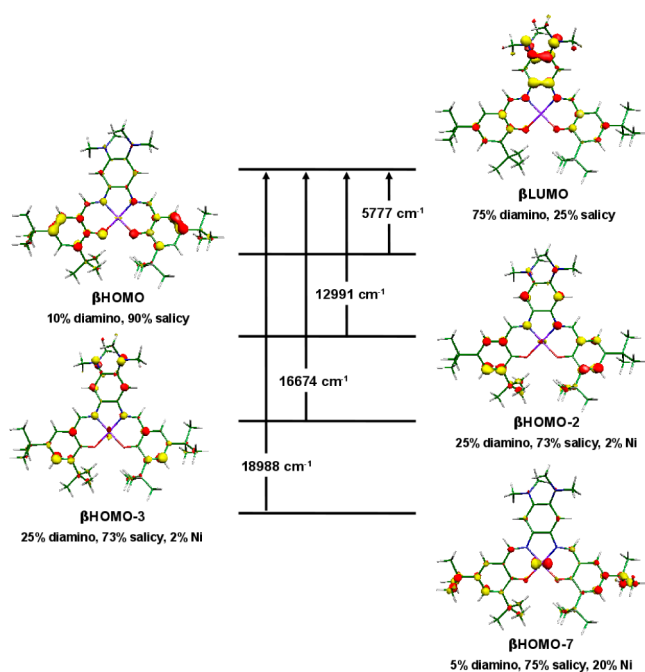


Figure 7. TD-DFT assignment of the main electronic excitations of singlet $^1\mathbf{I}^{2+}$, with fragment population of the relevant MOs. Fragments: Ni = nickel atom; salicy = salicylimine moieties (phenolate rings + imines); diamino = central ring + NMe₂ substituents.

β LUMO and β HOMO of $^1\mathbf{I}^{2+}$ have essentially the same character as those in \mathbf{I}^+ , but the relative energy of these orbitals in $^1\mathbf{I}^{2+}$ differ greatly from the situation in \mathbf{I}^+ . The highest oxidation state and nonradical nature of the central ring in \mathbf{I}^{2+} contributes to stabilization of β LUMO and leads to an overall red shift of the spectrum for \mathbf{I}^{2+} compared with \mathbf{I}^+ .

In the hypothetical triplet diradical $^3\mathbf{I}^{2+}$, the main electronic excitations arise from β HOMO \rightarrow β LUMO and β HOMO-1 \rightarrow β LUMO transitions (Figure 8). Similarly to nickel(II) phenoxyl radical salen complexes, the β HOMO \rightarrow β LUMO excitation corresponds to an IVCT, where both the donor and acceptor orbitals have strong phenolate-phenoxyl character.

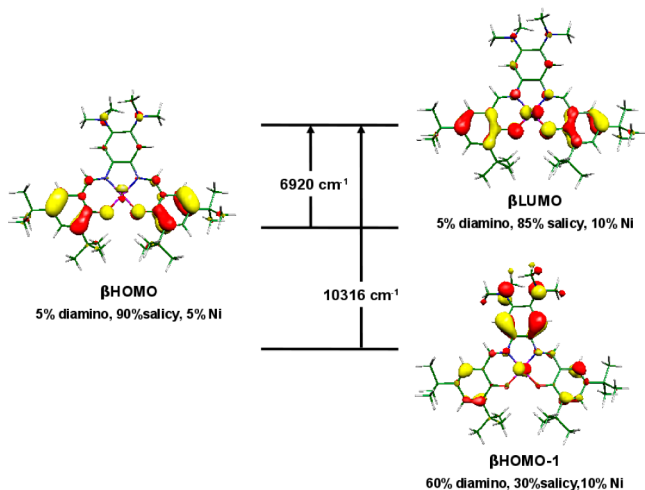


Figure 8. TD-DFT assignment of the main electronic excitations of triplet $^3\mathbf{I}^{2+}$, with fragment population of the relevant MOs. Fragments: Ni = nickel atom; salicy = salicylimine moieties (phenolate rings + imines); diamino = central ring + NMe₂ substituents.

According to previous studies,^{28–31} and consistent with the calculated oscillator strength of the 6920 cm^{−1} band, this transition should give rise to a very intense band in the NIR, in contrast to what is observed experimentally. This is again in favor of a singlet description for \mathbf{I}^{2+} .

Protonation Studies. By virtue of its NMe₂ substituents, complex \mathbf{I} can be protonated with a strong acid (HBF₄ or HSbF₆). The process was monitored by UV–vis spectroscopy (Figure 9) and yielded a complex with optical features similar

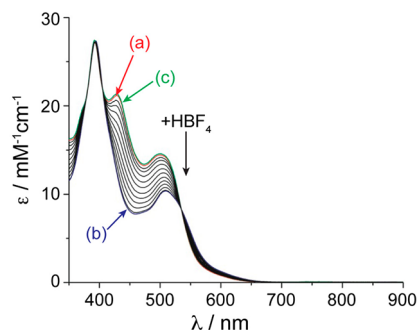


Figure 9. UV–vis titration of a CH₂Cl₂ solution of \mathbf{I} by HBF₄: (a, red) before the addition of acid; (b, blue) after the addition of 1 equiv of acid; (c, green) after the addition of 1 equiv of acid and 8 equiv of NEt₃. $l = 1.000$ cm. $T = 298$ K.

to those of \mathbf{I} , although less intense. The addition of a base to the acidic solution led to full recovery of the UV–vis features of \mathbf{I} , demonstrating the reversibility of the process. On a preparative scale, using HSbF₆ in methanol led to the isolation of crystals of $[\mathbf{1H}](\text{SbF}_6)$ that were suitable for X-ray diffraction analysis. The crystal structure of $[\mathbf{1H}](\text{SbF}_6)$ confirmed that protonation occurred on a NMe₂ group, with hydrogen bonding to the other (Figure 10). Consequently, the

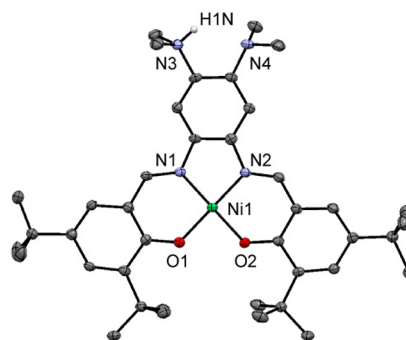


Figure 10. ORTEP representation at 50% ellipsoid probability of the cationic part of $[\mathbf{1H}](\text{SbF}_6)$. Hydrogen atoms, except the one located between the NMe₂ substituents, were omitted for clarity. Selected bond lengths: Ni1–N1 = 1.851(3) Å; Ni1–N2 = 1.864(3) Å; Ni1–O1 = 1.862(2) Å, Ni1–O2 = 1.852(2) Å.

NMe₂ groups are facing each other and are no longer related by a C₂ axis, as was the case in \mathbf{I} . The $\mathbf{1H}^+$ molecule is more planar than \mathbf{I} in their respective solid-state structure, with only a 8.3° angle between the carbon rings of each phenolate.

Protonation studies confirmed the involvement of the NMe₂ substituents in the redox behavior of \mathbf{I} . The CV of $\mathbf{1H}^+$ revealed a two-electron process (based on coulometry) with $E_p^{a1} = 0.57$ V and $E_p^{c1} = 0.21$ V (Figure 11). The protonation-induced increase by more than 300 mV of E_p^{a1} compared with

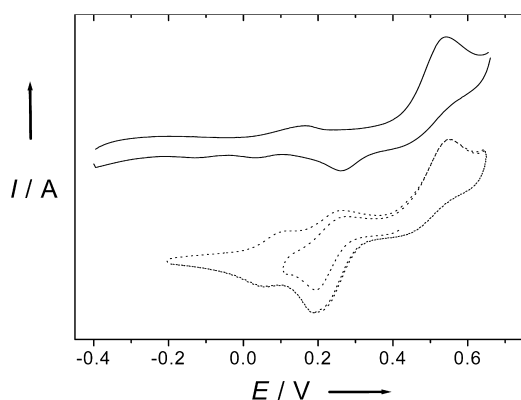
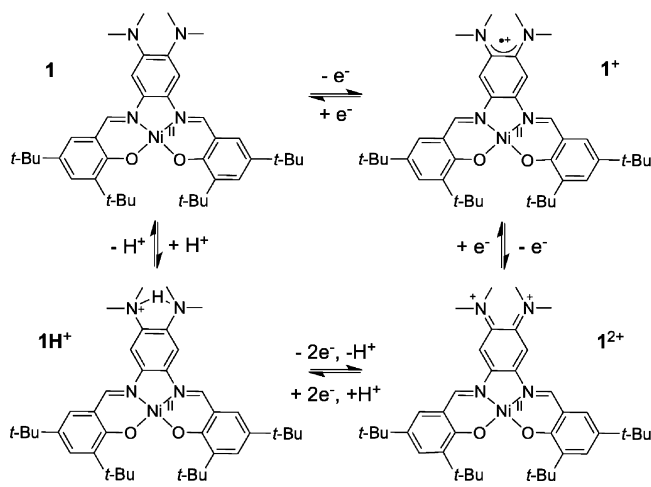


Figure 11. CV traces of 1 mM CH_2Cl_2 solutions (+0.1 M $n\text{Bu}_4\text{NClO}_4$) of 1H^+ before (—) and after (---) electrolysis at 0.6 V at a platinum working electrode. Potentials are relative to the Fc^+/Fc redox couple. Scan rates = 0.1 V/s. $T = 298$ K.

that of **1** is consistent with the NMe_2 substituents being significant contributors to the orbital from which the electron is abstracted in **1**. The large peak-to-peak separation, $\Delta E_p = 0.36$ V, indicates that a chemical reaction is coupled to electron transfer. The similarity between E_p^{cl} of 1H^+ and $E_{1/2}^2$ of **1** suggests that a significant amount of dication 1^{2+} (and likely monocation 1^+) is formed during oxidation of 1H^+ . In addition, the CV recorded after complete electrolysis at 0.6 V is not superimposable on that of 1H^+ and displays an additional feature at 0–0.3 V, which is reminiscent of the CV of **1** (Figure 11). These results suggest that oxidation of 1H^+ affords a transient acidic radical species that deprotonates readily to produce 1^+ . With the E_p^{al} value of 1H^+ being higher than $E_{1/2}^2$ of **1**, the net result is a two-electron oxidation of 1H^+ into 1^{2+} and proton release in solution (Scheme 3).

Scheme 3. Protonation/Oxidation Processes from **1**



The electrochemical oxidation of 1H^+ at 0.62 V (i.e., at a potential slightly higher than E_p^{al}) was monitored by EPR spectroscopy at 298 K. The EPR spectrum recorded at half-electrolysis (one electron removed) consisted of a signal very similar to the one of 1^+ , albeit much less intense (Figure S6 in the SI), while two-electron oxidation (complete electrolysis) resulted in a total quenching of the EPR signal. This behavior is consistent with 1^{2+} being the final oxidation product, with a small amount of 1^+ being transiently formed during electrolysis.

In order to confirm this oxidation scheme, we calculated the EPR parameters for putative protonated ($S = 1/2$) radical species 1H^{2+} by DFT methods (Figure S14 in the SI). The computed EPR parameters are $g_1 = 1.990$, $g_2 = 2.018$, and $g_3 = 2.049$ ($g_{\text{iso}} \sim 2.019$) without any HFC higher than 3 MHz, consistent with the location of the radical on the salicylimine moieties (Figure S13 in the SI). The poor agreement between these calculated values and the experimental data confirms that protonated radical species 1H^{2+} is not realistic under the experimental conditions.

UV–vis–NIR monitoring of the electrochemical oxidation of 1H^+ (0.62 V, two electrons removed) showed the appearance of absorption bands at 15100 and 18320 cm^{-1} indicating >95% formation of 1^{2+} (Figure S8 in the SI). All data thus suggest that the radical dication 1H^{2+} is very acidic. It is easily deprotonated, making oxidation of 1H^+ a proton-coupled two-electron transfer to afford 1^{2+} (Scheme 3).

CONCLUSION

In summary, the two NMe_2 substituents in salophen-type nickel(II) complex **1** direct the first two oxidation processes onto the central ring. Complex **1**, together with radical 1^+ and α -diiminoquinone 1^{2+} , constitute a rare example in the salophen family where the neutral part of the molecule, not the phenolates, gets oxidized by one³⁷ and two electrons reversibly. In these nickel(II) complexes, ligand **5** is thus found in three different oxidation states (2–, 1–, and 0) that are reversibly accessible at low redox potentials. We are currently studying the implications of the non-innocence of **5** onto the reactivity of its complexes with several other metal ions.

EXPERIMENTAL SECTION

Materials. Organics, solvents, and metal salts were obtained from commercial sources and used as received unless indicated otherwise. For oxidation studies, dichloromethane was degassed, dried over an MBraun solvent purification system, and then stored over activated 4 Å molecular sieves in amber bottles inside an inert-atmosphere glovebox (MBraun Labmaster) filled with a dry dinitrogen atmosphere (less than 1 ppm in dioxygen and water). Compound **2**¹⁷ and 3,5-di-*tert*-butylsalicylaldehyde³⁸ were synthesized following literature procedures.

Characterization. Elemental CHN microanalyses were performed by the Microanalytical Service of the Institut de Chimie des Substances Naturelles (CNRS, France). Solution ^1H and ^{13}C NMR spectra were recorded on a Varian Innova 500 MHz instrument using tetramethylsilane as the internal reference. Fourier transform infrared (FT-IR) spectra were recorded on a Perkin-Elmer 882 spectrophotometer as KBr pellets. UV–vis–NIR solution spectra were recorded on Varian CARY SE (250–1400 nm) and 5000 (1400–3300 nm) spectrophotometers. X-band EPR spectra were recorded on a Bruker EMX Plus spectrometer controlled with *Xenon* software and equipped with a Bruker teslameter. A Bruker nitrogen-flow cryostat connected to a high-sensitivity resonant cavity was used for 100 K measurements. An Oxford Instrument helium-flow cryostat connected to a dual-mode resonant cavity was used to run experiments at 25 K. The spectra were simulated using *SIMFONIA* software (Bruker). Cyclic voltammetry curves were recorded on a CHI 620 potentiostat in a standard three-electrode cell under an argon atmosphere. Electrochemical measurements were performed at either 298 K for the nonoxidized complexes or 243 K for the oxidized species to ensure as little decomposition as possible. An AgNO_3/Ag (0.01 M) reference electrode was used. All of the potentials given in the text refer to the regular Fc^+/Fc redox couple used as the external reference. A vitreous carbon disk electrode (3 mm diameter) or a platinum disk (2 μm diameter) polished with 1 mm diamond paste was used as the working electrode. Both the carbon and platinum working electrodes gave the same response for **1**. In the case

of IH^+ , we observed significant deposition at the carbon working electrode, which was avoided by using a platinum one. Electrolysis was performed on a PAR 273 potentiostat, under an argon atmosphere at -40°C . The setup for bulk electrolyses consisted of a carbon felt electrode (for **1**) or a large platinum grid (for IH^+), with the counter electrode isolated by a salt bridge. RDE voltammetry was performed with a Radiometer TCV101 speed control unit and an EDI 101 electrode.

X-ray Crystallography. Crystallographic analysis was performed using the microfocus Cu $K\alpha$ source of a Bruker APEX-DUO diffractometer. The frames were integrated with the Bruker SAINT software package using a narrow-frame algorithm. Data were corrected for absorption effects using the multiscan method (SADABS). The structures were solved by direct methods and refined using the Bruker APEX2 software package (SHELXL instructions).³⁹ All non-hydrogen atoms were refined with anisotropic thermal parameters. Hydrogen atoms were generated in idealized positions, riding on the carrier atoms with isotropic thermal parameters, except for H1N in $[\text{IH}](\text{SbF}_6)$, which was located on the electronic density difference map and allowed to refine with only a distance restraint from N3.

Computational Details. All theoretical calculations were performed with the ORCA program package.⁴⁰ Full geometry optimizations were carried out for all complexes using the GGA functional BP86^{41–43} in combination with the TZV/P⁴⁴ basis set for all atoms and by taking advantage of the resolution of the identity (RI) approximation in the Split-RI-J variant⁴⁵ with the appropriate Coulomb fitting sets.⁴⁶ Increased integration grids (Grid4 in the ORCA convention) and tight self-consistent-field convergence criteria were used. Solvent effects were accounted for according to the experimental conditions. For that purpose, we used the CH_2Cl_2 ($\epsilon = 9.08$) solvent within the framework of the conductor-like screening (COSMO) dielectric continuum approach.⁴⁷ The relative energies were obtained from single-point calculations using the B3LYP^{48,49} functional together with the TZV/P⁴⁴ basis set. They were computed from the gas-phase-optimized structures as a sum of the electronic energy, thermal corrections to free energy, and free energy of solvation. Optical properties were also obtained from single-point calculations using the hybrid functional B3LYP^{48,49} and the TZV/P⁴⁴ basis set. Electronic transition energies and dipole moments for all models were calculated using TD-DFT^{50–52} within the Tamm-Dancoff approximation.^{53,54} To increase the computational efficiency, the RI approximation⁵⁵ was used in calculating the Coulomb term and at least 30 excited states were calculated in each case. \mathbf{g} tensors and HFC constants were obtained from single-point calculations employing the hybrid functional B3LYP.^{48,49} The triply polarized core property basis set CP(PPP)⁵⁶ was applied for the metal, while the EPR-II⁵⁷ basis set was used for all remaining atoms. Special care was also taken to ensure accurate results by increasing the size of the integration grid to 7 (ORCA convention) for the metal center.⁵⁶

Syntheses. **4,5-Bis(dimethylamino)-1,2-dinitrobenzene (3).** To a degassed suspension of **2**¹⁷ (5.5 g, 27.7 mmol) and paraformaldehyde (8.3 g, 276 mmol) in glacial acetic acid (50 mL) was added sodium cyanoborohydride (8.75 g, 139 mmol) in small portions. The suspension was then stirred overnight at room temperature under an inert atmosphere. The solid was filtered off and rinsed with acetone. The filtrate was evaporated to dryness, and dichloromethane and water were added. The product was extracted two times, and the combined organic phases were washed once with water, dried over sodium sulfate, and evaporated to dryness. The resulting oil was dissolved in 50 mL of diethyl ether, filtered over cotton, and evaporated to a minimum. A total of 500 mL of cold hexanes was added, and the suspension was kept in a -20°C freezer overnight to yield a dark-red crystalline material that was filtered off and dried under vacuum. Yield: 6.25 g, 89%. Anal. Calcd for $\text{C}_{10}\text{H}_{14}\text{N}_4\text{O}_4$ (254.2 g/mol): C, 47.24; H, 5.55; N, 22.04. Found: C, 46.88; H, 5.53; N, 21.92. ^1H NMR (CDCl_3 , 500 MHz): δ 2.87 (s, 12H), 7.21 (s, 2H). ^{13}C NMR (CDCl_3 , 125 MHz): δ 40.41, 113.62, 136.43, 146.73. FT-IR (KBr): ν 1505, 1520, 1544, 1572, 1582 (NO_2) cm^{-1} .

N^1,N^1,N^2,N^2 -Tetramethylbenzene-1,2,4,5-tetramine (4). A suspension of **3** (1.02 g, 4 mmol) and 10% Pd/C (0.1 g) in methanol (80

mL) was stirred under a dihydrogen atmosphere at room temperature either overnight under 40 bar of pressure in a stainless steel autoclave or for 3 days under 40 psi of pressure in a Parr shaker. The suspension was then filtered under an inert atmosphere over a pad of Celite that was rinsed well with degassed methanol. Removal of the solvent yielded a light-brown, air-sensitive solid. ^1H NMR ($\text{DMSO}-d_6$, 500 MHz): δ 3.34 (s, 12H), 4.07 (s, 4H), 6.20 (s, 2H).

4,5-Bis(dimethylamino)benzene-1,2-bis(3,5-di-*tert*-butylsalicylimine) (5). After rinsing the Celite in the precedent synthesis (without isolating the product), the methanolic solution of **4** was directly added to a degassed solution of 3,5-di-*tert*-butylsalicylaldehyde³⁸ (2.0 g, 8.5 mmol) and trimethylorthoformate (6.5 mL) in methanol (50 mL). After reflux for 24 h under an inert atmosphere, the suspension was cooled with an ice bath. The air-stable solid was filtered off, and excess trimethylorthoformate was removed by twice-repeated redissolution in a small amount of dichloromethane followed by evaporation to dryness in a rotary evaporator. The orange solid was then collected with cold methanol, filtered off, rinsed twice with cold methanol, and dried under vacuum. Yield: 1.7 g, 67% over two steps. Anal. Calcd for $\text{C}_{40}\text{H}_{58}\text{N}_4\text{O}_2$ (626.9 g/mol): C, 76.63; H, 9.33; N, 8.94. Found: C, 76.59; H, 9.43; N, 8.79. ^1H NMR (CDCl_3 , 500 MHz): δ 1.30 (s, 18H, *t*-Bu), 1.42 (s, 18H, *t*-Bu), 2.85 (s, 12H, NCH_3), 6.73 (s, 2H, central aromatic), 7.18 (d, 2H, 2.4 Hz, phenol), 7.38 (d, 2H, H_α , 2.4 Hz, phenol), 8.62 (s, 2H, imine), 13.80 (s, 2H, OH). ^{13}C NMR (CDCl_3 , 125 MHz): δ 29.47, 31.51, 34.16, 35.10, 41.47, 109.34, 118.63, 126.39, 127.45, 135.84, 136.99, 140.04, 144.61, 158.36, 162.34. FT-IR (KBr): ν 1584, 1614 ($\text{C}=\text{N}$) cm^{-1} .

1: To a solution of **5** (313 mg, 0.5 mmol) in dichloromethane (5 mL) was added dropwise a methanolic solution (20 mL) of nickel(II) acetate tetrahydrate (88.4 mg, 0.5 mmol). After 1 h of reflux, the suspension was cooled. The precipitate was filtered off and rinsed copiously with methanol. A pure material was obtained as a red fraction upon short filtration over silica eluted by dichloromethane. The fraction was then concentrated to ca. 5 mL and layered with methanol to afford a red crystalline product. Yield: 328 mg, 96%. Anal. Calcd for $\text{C}_{40}\text{H}_{56}\text{N}_4\text{NiO}_2$ (683.6 g/mol): C, 70.28; H, 8.26; N, 8.20. Found: C, 70.24; H, 8.29; N, 8.15. ^1H NMR (CDCl_3 , 500 MHz): δ 1.29 (s, 18H, *t*-Bu), 1.45 (s, 18H, *t*-Bu), 2.86 (s, 12H, CH_3), 7.02 (s, 2H, central aromatic), 7.07 (d, 2H, 2 Hz, phenol), 7.35 (d, 2H, 2 Hz, phenol), 7.96 (s, 2H, imine). ^{13}C NMR (CDCl_3 , 125 MHz): δ 29.73, 31.30, 33.92, 35.91, 41.49, 102.67, 119.66, 126.35, 129.75, 136.43, 136.80, 140.39, 144.79, 152.12, 163.79. FT-IR (KBr): ν 1501, 1526, 1605 ($\text{C}=\text{N}$) cm^{-1} . Needle-shaped single crystals amenable for X-ray crystallography were grown by the slow diffusion of a methanol layer atop a dichloromethane solution of **1**.

$[\text{IH}](\text{SbF}_6)$: Atop a solution of **1** (50 mg, 0.073 mmol) in dichloromethane (5 mL) was carefully layered a solution of $\text{HSbF}_6 \cdot 6\text{H}_2\text{O}$ (48 mg, 0.146 mmol) in 15 mL of methanol. The mixture was allowed to diffuse and evaporate slowly, yielding a deep-red crystalline solid that was washed with dichloromethane. Single crystals were selected from this solid for X-ray diffraction studies.

Diacetylferrocenium hexafluoroantimonate ($\text{Ac}_2\text{FcSbF}_6$) was prepared in the glovebox by stirring equimolar amounts of recrystallized diacetylferrocene (Ac_2Fc ; 270.1 mg, 1.0 mmol) and AgSbF_6 (343.62 mg, 1.0 mmol) in diethyl ether (10 mL) for 20 min. The dark-blue precipitate was filtered off over a small plug of Celite and was rinsed well with ether. The titled compound was then extracted off the plug by dichloromethane, yielding solutions of ca. 7 mM concentration. The titled compound can be isolated by rotary evaporation, but for purity reasons, we preferred the use of freshly prepared solutions. The exact concentration of these solutions was assessed by UV–vis titration experiments of **1**.

■ ASSOCIATED CONTENT

● Supporting Information

Additional electrochemical, EPR, UV–vis–NIR, and DFT data, together with crystallographic CIF files (CCDC 893505 and 893506). This material is available free of charge via the Internet at <http://pubs.acs.org>.

■ AUTHOR INFORMATION

Corresponding Author

*E-mail: dr.x@concordia.ca (X.O.), fabrice.thomas@ujf-grenoble.fr (F.T.).

Author Contributions

All authors have given approval to the final version of the manuscript.

Notes

The authors declare no competing financial interest.

■ ACKNOWLEDGMENTS

This work was funded by the CNRS (France) and by an NSERC Discovery grant (Canada). X-ray diffraction data were collected on a CFI-funded infrastructure (Canada).

■ REFERENCES

- (1) Lyaskovskyy, V.; de Bruin, B. *ACS Catal.* **2012**, *2*, 270–279.
- (2) Chirik, P. J.; Wieghardt, K. *Science* **2010**, *327*, 794–795.
- (3) Ortiz de Montellano, P. R. *Chem. Rev.* **2010**, *110*, 932–948.
- (4) Kaim, W.; Schwederski, B. *Coord. Chem. Rev.* **2010**, *254*, 1580–1588.
- (5) Kaim, W. *Inorg. Chem.* **2011**, *50*, 9752–9765.
- (6) Kadish, K. M.; Caemelbecke, E. V.; Royal, G. In *The Porphyrin Handbook*; Kadish, K. M., Smith, K. M., Guillard, R., Eds.; Academic Press: London, 2000; pp 1–114.
- (7) Chaudhuri, P.; Wieghardt, K. *Prog. Inorg. Chem.* **2001**, *50*, 151–216.
- (8) Thomas, F. *Eur. J. Inorg. Chem.* **2007**, 2379–2404.
- (9) Pierpont, C.; Lange, C. *Prog. Inorg. Chem.* **1994**, *41*, 331–442.
- (10) Chaudhuri, P.; Verani, C. N.; Bill, E.; Bothe, E.; Weyhermüller, T.; Wieghardt, K. *J. Am. Chem. Soc.* **2001**, *123*, 2213–2223.
- (11) Ray, K.; Petrenko, T.; Wieghardt, K.; Neese, F. *Dalton Trans.* **2007**, 1552–1566.
- (12) Gordon-Wylie, S. W.; Claus, B. L.; Horwitz, C. P.; Leychik, Y.; Workman, J. M.; Marzec, A. J.; Clark, G. R.; Rickard, C. E. F.; Conklin, B. J.; Sellers, S.; Yee, G. T.; Collins, T. J. *Chem.—Eur. J.* **1998**, *4*, 2173–2181.
- (13) Aukauloo, A.; Ottenwaelde, X.; Ruiz, R.; Poussereau, S.; Pei, Y.; Journaux, Y.; Fleurat, P.; Volatron, F.; Cervera, B.; Muñoz, M. C. *Eur. J. Inorg. Chem.* **1999**, 1067–1071.
- (14) Ottenwaelde, X.; Ruiz-García, R.; Blondin, G.; Carasco, R.; Cano, J.; Lexa, D.; Journaux, Y.; Aukauloo, A. *Chem. Commun.* **2004**, 504–505.
- (15) Ottenwaelde, X.; Aukauloo, A.; Journaux, Y.; Carrasco, R.; Cano, J.; Cervera, B.; Castro, I.; Curreli, S.; Muñoz, M. C.; Roselló, A. L.; Soto, B.; Ruiz-García, R. *Dalton Trans.* **2005**, 2516–2526.
- (16) Tondreau, A. M.; Milsman, C.; Patrick, A. D.; Hoyt, H. M.; Lobkovsky, E.; Wieghardt, K.; Chirik, P. J. *J. Am. Chem. Soc.* **2010**, *132*, 15046–15059.
- (17) Cheeseman, G. W. H. *J. Chem. Soc.* **1962**, 1170.
- (18) Berg, K. E.; Pellegrin, Y.; Blondin, G.; Ottenwaelde, X.; Journaux, Y.; Moragues Canovas, M.; Mallah, T.; Parsons, S.; Aukauloo, A. *Eur. J. Inorg. Chem.* **2002**, 323–325.
- (19) Lassalle-Kaiser, B.; Guillot, R.; Aukauloo, A. *Tetrahedron Lett.* **2007**, *48*, 7004–7006.
- (20) Rotthaus, O.; Jarjays, O.; Philouze, C.; Pérez Del Valle, C.; Thomas, F. *Dalton Trans.* **2009**, 1792–1800.
- (21) Benisvy, L.; Kannappan, R.; Song, Y.; Milikisyants, S.; Huber, M.; Mutikainen, I.; Turpeinen, U.; Gamez, P.; Bernasconi, L.; Baerends, E. J.; Hartl, F.; Reedijk, J. *Eur. J. Inorg. Chem.* **2007**, 637–642.
- (22) Rotthaus, O.; Thomas, F.; Jarjays, O.; Philouze, C.; Saint-Aman, E.; Pierre, J. *Chem.—Eur. J.* **2006**, *12*, 6953–6962.
- (23) Thomas, F.; Jarjays, O.; Duboc, C.; Philouze, C.; Saint-Aman, E.; Pierre, J. *Dalton Trans.* **2004**, 2662–2669.
- (24) Elbl-Weiser, K.; Krieger, C.; Staab, H. A. *Angew. Chem., Int. Ed. Engl.* **1990**, *29*, 211–213.
- (25) Barth, T.; Krieger, C.; Neugebauer, F. A.; Staab, H. A. *Angew. Chem., Int. Ed. Engl.* **1991**, *30*, 1028–1030.
- (26) Elbl, K.; Krieger, C.; Staab, H. A. *Angew. Chem., Int. Ed. Engl.* **1986**, *25*, 1023–1024.
- (27) Shimazaki, Y.; Tani, F.; Fukui, K.; Naruta, Y.; Yamauchi, O. *J. Am. Chem. Soc.* **2003**, *125*, 10512–10513.
- (28) Storr, T.; Wasinger, E. C.; Pratt, R. C.; Stack, T. D. P. *Angew. Chem., Int. Ed.* **2007**, *46*, 5198–5201.
- (29) Shimazaki, Y.; Stack, T. D. P.; Storr, T. *Inorg. Chem.* **2009**, *48*, 8383–8392.
- (30) Shimazaki, Y.; Arai, N.; Dunn, T. J.; Yajima, T.; Tani, F.; Ramogida, C. F.; Storr, T. *Dalton Trans.* **2011**, *40*, 2469–2479.
- (31) Chiang, L.; Kochem, A.; Jarjays, O.; Dunn, T. J.; Vezin, H.; Sakaguchi, M.; Ogura, T.; Orio, M.; Shimazaki, Y.; Thomas, F.; Storr, T. *Chem.—Eur. J.* **2012**, *18*, 14117–14127.
- (32) Connelly, N. G.; Geiger, W. E. *Chem. Rev.* **1996**, *96*, 877–910.
- (33) Neugebauer, F. A.; Funk, B.; Staab, H. A. *Tetrahedron Lett.* **1994**, *35*, 4755–4758.
- (34) In general, nickel(II) phenoxyl radical salen complexes are easily converted into the octahedral nickel(III) bis(phenolate) valence isomer in coordinating solvents (such as methanol). Dissolution of 1^+ in a $\text{CH}_2\text{Cl}_2/\text{CH}_3\text{OH}$ (3:1) mixture (precipitation is observed when higher amounts of CH_3OH are used) does not result in a significant change of the EPR spectrum compared to neat CH_2Cl_2 (Figure S5 in the SI).
- (35) Orio, M.; Jarjays, O.; Kanso, H.; Philouze, C.; Neese, F.; Thomas, F. *Angew. Chem., Int. Ed.* **2010**, *49*, 4989–4992.
- (36) Speiser, B.; Würde, M.; Maichle-Mössner, C. *Chem.—Eur. J.* **1998**, *4*, 222–233.
- (37) Kochem, A.; Jarjays, O.; Baptiste, B.; Philouze, C.; Vezin, H.; Tsukidate, K.; Tani, F.; Orio, M.; Shimazaki, Y.; Thomas, F. *Chem.—Eur. J.* **2012**, *18*, 1068–1072.
- (38) Larrow, J.; Jacobsen, E. *Org. Synth.* **1998**, *75*, 1–11.
- (39) Sheldrick, G. M. *SHELXL-97, Program for Crystal Structure Refinement*; University of Göttingen: Göttingen, Germany, 1997; <http://shelx.uni-ac.gwdg.de/SHELX/index.html>.
- (40) Neese, F. *ORCA—an ab initio, Density Functional and Semiempirical Program Package*, version 2.8.0; Universität Bonn: Bonn, Germany, 2010.
- (41) Perdew, J. *Phys. Rev. B* **1986**, *33*, 8822–8824.
- (42) Perdew, J. *Phys. Rev. B* **1986**, *34*, 7406–7406.
- (43) Becke, A. *Phys. Rev. A* **1988**, *38*, 3098–3100.
- (44) Schäfer, A.; Huber, C.; Ahlrichs, R. *J. Chem. Phys.* **1994**, *100*, 5829–5835.
- (45) Neese, F. *J. Comput. Chem.* **2003**, *24*, 1740–1747.
- (46) Weigend, F. *Phys. Chem. Chem. Phys.* **2006**, *8*, 1057–1065.
- (47) Klamt, A.; Schüürmann, G. *J. Chem. Soc., Perkin Trans. 2* **1993**, 799–805.
- (48) Becke, A. *J. Chem. Phys.* **1993**, *98*, 5648–5652.
- (49) Lee, C.; Yang, W.; Parr, R. *Phys. Rev. B* **1988**, *37*, 785–789.
- (50) Casida, M. E. In *Recent Advances in Density Functional Methods*; Chong, D. P., Ed.; World Scientific: Singapore, 1995.
- (51) Stratmann, R.; Scuseria, G.; Frisch, M. J. *J. Chem. Phys.* **1998**, *109*, 8218–8224.
- (52) Bauernschmitt, R.; Ahlrichs, R. *Chem. Phys. Lett.* **1996**, *256*, 454–464.
- (53) Hirata, S.; Head-Gordon, M. *Chem. Phys. Lett.* **1999**, *314*, 291–299.
- (54) Hirata, S.; Head-Gordon, M. *Chem. Phys. Lett.* **1999**, *302*, 375–382.
- (55) Neese, F.; Olbrich, G. *Chem. Phys. Lett.* **2002**, *362*, 170–178.
- (56) Neese, F. *Inorg. Chim. Acta* **2002**, *337*, 181–192.
- (57) Barone, V. In *Recent Advances in Density Functional Methods*; Chong, D. P., Ed.; World Scientific: Singapore, 1996.